The Astrophysical Journal Letters, 925:L11 (7pp), 2022 February 1 https://doi.org/10.3847/2041-8213/ac4b62

Discerning between Different 'Oumuamua Models by Optical and Infrared Observations

Eirik G. Flekkøy and Joachim F. Brodin
CoE PoreLab, the Njord Centre, Department of Physics, University of Oslo, P.O. Box 1048, Blindern, N-0316, Oslo, Norway; e.g.flekkoy@fys.uio.no
Received 2021 December 22; revised 2022 January 12; accepted 2022 January 13; published 2022 January 27

Abstract

The first interstellar object to be observed in our solar system, 1I/2017 U1 'Oumuamua, combines the lack of observable cometary activity with an extra-gravitational acceleration. This has given rise to several mutually exclusive explanations based on different assumptions in the material composition of 'Oumuamua. We show how a combination of observations in the infrared and optical spectra may serve to distinguish between these explanations once another object with 'Omuamua-like properties comes close enough to Earth. This possibility is linked to the widely different thermal properties of the different material models that have been proposed. Developing a model for the thermal conduction and infrared signal from a fractal model, we compare predictions of the infrared signal with that from standard thermal models that assume 'Oumuamua to be either a solid piece of rock/ice or a thin sheet.

Unified Astronomy Thesaurus concepts: Small Solar System bodies (1469)

1. Introduction

Since the first known interstellar object 1I/2017 U1 ('Oumuamua) was discovered in 2017 October, much effort has gone into explaining its formation and unusual behavior (Ćuk 2018; Raymond et al. 2018; Bannister et al. 2019; Luu et al. 2020). This behavior is characterized by lack of cometary activity (Jewitt et al. 2017; Meech et al. 2017), a highly elongated shape (Luu et al. 2019), and a size that is unexpected from estimated distributions of small bodies in the solar system or a protoplanetary disk (Jewitt et al. 2017; Moro-Martín 2018, 2019)—as well as nongravitational acceleration (Micheli et al. 2018). We recently suggested that 'Oumuamua originated as a cosmic "dust-bunny," a cometary fractal aggregate (CFA) that was formed in a cometary tail (Flekkøy et al. 2019; Luu et al. 2020). Others (Ćuk 2018; Fitzsimmons et al. 2018) have proposed that it is a potentially volatile substance covered by a rocky crust that was formed by tidal disruption and heating during a close encounter with a nearby star (Ćuk 2018). Another suggestion is that it is a chunk of frozen N_2 ejected from an exo-Pluto-like surface (Desch & Jackson 2021; Jackson & Desch 2021), or a piece of pure H_2 ice (Seligman & Laughlin 2020). Finally, the possibility that it is a light sail developed by an alien civilization has been advocated (Bialy & Loeb 2018). Since 'Omuamua itself is no longer observable, deciding between these models must await the next passage of a similar object. Here we show that the combination of optical and infrared observations offers such a distinction possibility if the passage of the next object is as close to earth as was 'Oumuamua.

We shall refer to these models as the CFA-, ice- rock- and light-sail model. In the case of the CFA and light-sail models, radiation pressure from the Sun may account for nongravitational acceleration. However, an object of solid ice or rock is too massive to be affected by radiation pressure, and the nongravitational acceleration is explained by undetectable outgassing. The same explanation has been applied in the case where the sublimating substance is covered by a rocky crust (Zhang & Lin 2020).

Infrared observations of 'Oumuamua were limited to those of the Spitzer telescope, which had run out of cooling helium (Trilling et al. 2018). The new James Webb Space Telescope, to be located at the second Lagrange point, will offer increased resolution in the infrared spectrum. Provided the size and closest distance to Earth is comparable to that of 'Oumuamua, the combination of optical and infrared observations of another such object would then be sufficient to distinguish between the models. It would require that the optical observations constrain the shape and rotational state of the object, as was the case with 'Oumuamua (Jewitt et al. 2017; Jewitt & Luu 2019; Luu et al. 2019; Mashchenko 2019), even though it had passed its closest encounter with Earth by the time it was first observed on UT 2017 October 18.5 (Williams 2017).

In this case the infrared signature would be qualitatively different for the different models since these have different thermal properties: during observation of the night side, a rock surface will gradually cool. A CFA, by contrast, is partially transparent to the infrared radiation owing to its high thermal conductivity, and will gradually heat on the night side. A surface made of N_2 ice will stay too cold for detection at all, and, finally, a light sail is so thin that it has the same infrared signature on both sides.

2. Thermal Models

As a test case of these distinction possibilities, we take the rotational state and observation geometry to be as simple as possible, and use the known values of Earth distance, size, and shape estimates of 'Oumuamua.

In all models, the shape is taken to be enveloped by an ellipsoid with semimajor axis $a = 119$ m, $b = 111$ m, and $c = 19$ m (see Mashchenko 2019) exposing the widest surface area toward the incoming light during its rotation. The angular velocity $\omega = 2\pi/7$h is that of 'Oumuamua and points in the direction normal to the plane of Figure 1.

In the ice model, the absorbed radiation energy from the Sun is consumed by sublimation at a constant sublimation temperature, while in the other models, it is transported as

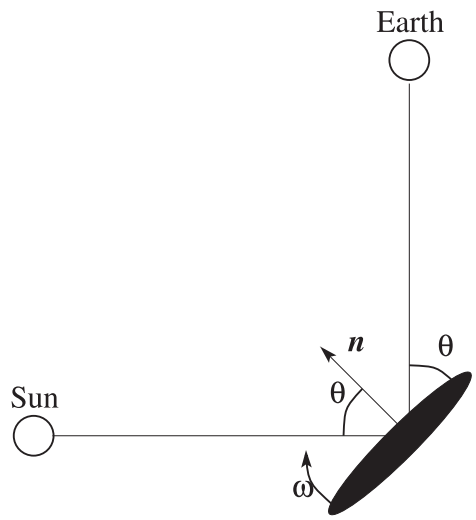

Figure 1. Top view of the observational geometry showing an oblate ellipsoid facing the Sun and Earth with its broadside during its rotation. The phase angle is 90′ and θ the angle of incident light to the surface normal $\boldsymbol{n}$. The in-plane rotation is given by the angular velocity ω.

heat below the surface. In the CFA model, the dominant mode of this transport is by photons, while in the light-sail and rock models, it is by phonons.

The formation scenario of the rock model is suggested to involve extensive tidal fragmentation of a volatile rich parent body during a close H_2O ice encounter with its host stars followed by ejection (Zhang & Lin 2020). The heating during this process would have created a solid crust of unknown permeability surrounding a more volatile interior. In calculating the surface temperature, we shall neglect the effect of these volatiles sublimating and only consider the diffusive heat transport into a regolith surface.

Porous materials found in the regoliths of asteroids and comets have much smaller values of the thermal conductivity and diffusivity than normal rocks, a typical value being $\kappa_t = 10^{-2}$ W/(m K) and $D_t = 10^{-8}$ m^2 s^{-1} (see Cooper et al. 2003 and Jewitt et al. 2017), and even smaller values are assumed by some authors (Zhang & Lin 2020). For this reason, the thermal diffusion length in the rock model is ∼cm, which is much smaller than the thickness $2c$.

The surface temperature of the rock model is obtained by thermal modeling (Fitzsimmons et al. 2018) based on the heat diffusion equation

$$\frac{\partial T}{\partial t} = D_t \frac{\partial T}{\partial z^2} \tag{1}$$

which is solved subject to the boundary conditions

$$(1 - p) j_{\rm sun} \cos\theta = -\kappa_t \frac{\partial T(0, t)}{\partial z} + \sigma T^4(0, t)$$
$$0 = -\kappa_t \frac{\partial T(L, t)}{\partial z} + \sigma T^4(L, t) \tag{2}$$

where $p \sim 0.1$ is the albedo and $j_{\rm sun} = 1360\,{\rm W\,m^{-2}}$ the solar influx at a distance $R = 1$ au, L is the thickness in the z-direction normal to the surface, and κ_t is the thermal conductivity. Compared to the standard thermal model (NEATM Harris 1998) this description does not include the beaming effect (beaming factor $\eta = 1$), but does include the effect of finite thermal inertia. The thermal diffusivity $D_t = \kappa_t / c_v$, where c_v is the heat capacity per unit volume.

The first of the above equations describes the day side and the last the night side. When $\cos\theta < 0$, boundary conditions for $z = 0$ and $z = L$ are interchanged, reflecting the fact that the day and night sides are interchanged. The above equations are integrated using a simple finite-difference scheme and $\theta = \omega t$.

For the frozen N_2, the temperature is simply taken to be the sublimation temperature at zero pressure, $T \approx 63$ K. In the light-sail model, the internal diffusive transport of heat may be neglected and the temperature assumed to be the same on both sides as such a sail would have to be much thinner than any reasonable diffusion length. The temperature is then obtained from the energy balance

$$j_{\rm sun} \cos\theta = 2\sigma T^4 \tag{3}$$

where the factor 2 comes from the fact that the sail would radiate equally on both sides.

2.1. Thermal Conduction in a Fractal

While the temperature evolution in the ice-sail and rock model is described by well established thermal models, the corresponding transport equations of heat in a fractal structure are less well established. Diffusion on fractals has been studied extensively (O'Shaughnessy & Procaccia 1985; Havlin & Ben-Avraham 2002; Olsen et al. 2019). In our case, however, the transport is not restricted to the fractal itself, but rather it occurs by radiation in the open space between the solid sites on the fractal.

In Appendix A.2 we show that the mean free path of a photon originating from an arbitrary location inside the fractal structure is $\overline{\lambda} = (4\pi r_0/3)(a/r_0)^{3-D}$ where $D = 2.35$ (Flekkøy et al. 2019) is the fractal dimension and r_0 the radius of the particles that make up the fractal. A photon originating from such a solid particle, by contrast, has a mean free path $\sim r_0$, that is much smaller than $\overline{\lambda}$. For this reason, we may take the radiation field and solid structure to be in local equilibrium. In other words, they will have the same temperature in the vicinity of the solid structure.

On average, the radiation field then has a constant temperature in every plane normal to the surface and there will be a temperature gradient in the direction $\boldsymbol{n}$. The radiation across a given plane normal to $\boldsymbol{n}$ will be re-absorbed over a distance $\overline{\lambda}$, so that the net energy flux j_t passing from z to $z + \overline{\lambda}$ is

$$j_t = \sigma(T^4(z) - T^4(z + \overline{\lambda})), \tag{4}$$

where $\sigma = 5.67\,10^{-8}$ W/(m^{2}K^4) is the Stefan–Boltzmann constant. Taylor expansion of the above expression yields

$$j_t \approx -\sigma \frac{\partial T^4}{\partial z} \overline{\lambda} = -\kappa_t \frac{\partial T}{\partial z} \tag{5}$$

where the thermal conductivity

$$\kappa_t = \frac{16}{3} r_0 \sigma T^3 \left(\frac{a}{r_0}\right)^{3-D} \approx 0.8 {\rm W/(K\ m)} \tag{6}$$

if the values $r_0 = 1\mu$ m and $T = 250$ K are used (Flekkøy et al. 2019). This value is in the range of the thermal conductivity $\kappa_0 \sim 1$ W/(K m) for silicate rocks.

By contrast, the thermal conductivity κ_s of the solid structure that makes up the fractal depends on the solid fraction

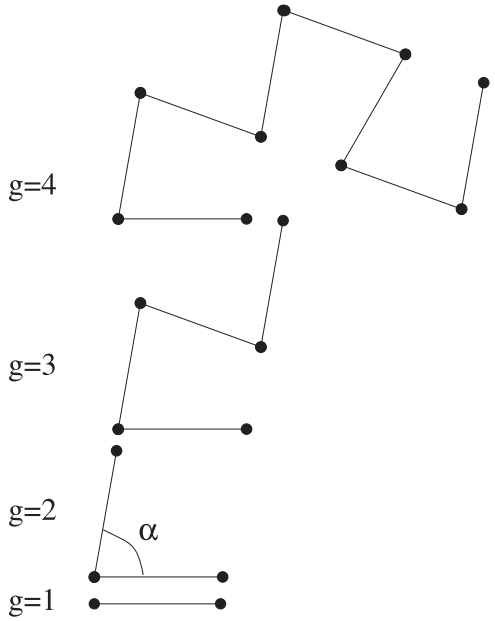

Figure 2. The first four generations of the fractal model structure.

$\phi_s = (r_0/a)^{3-D} \sim 10^{-5}$(Flekkøy et al. 2019) through the relation $\kappa_s = \phi_s \kappa_0 \sim 10^{-5}$ W/(Km). This means that the thermal conduction of the radiation field is ∼5 orders of magnitude larger than that of the solid.

The heat capacity per unit volume of the radiation field is given as $c_v = \partial\epsilon/\partial T$ where the energy density $\epsilon = \sigma T^4/c_0$, and c_0 is the speed of light. It may be written

$$c_v = \frac{1}{c_0}\frac{\partial j}{\partial T} = \frac{4\sigma T^3}{c_0} \approx 1.2\ 10^{-8}\ \mathrm{J/(m^3K)} \tag{7}$$

where $j = \sigma T^4$. This value is 8–9 orders of magnitude smaller than the average heat capacity of the solid, which is given as

$$c_{vs} = c_{v0}\phi_s \approx 5\ \mathrm{J/(m^3K)} \tag{8}$$

where $c_{v0} \sim 10^6\ \mathrm{J/(m^3K)}$ is the typical heat capacity of rocks. So, while the radiation field governs the heat conductivity, the solid phase governs the heat capacity, as was also found by Merril (Merril 1969) who studied heat transfer in evacuated powders. As a result, the thermal diffusivity

$$D_t = \frac{\kappa_t}{c_{vs}} \approx 0.14\ \mathrm{m^2 s^{-1}}. \tag{9}$$

The corresponding thermal diffusion length in the CFA over a time $t = 3.5$ h (the half-period of 'Oumuamua) $x_t = \sqrt{2D_t t} \approx$ 60 m, which is significantly larger than the estimated thickness $2c = 38$ m (Mashchenko 2019).

This implies a transparency to infrared radiation, which will vary with location. Since any fractal structure has inhomogeneities on all length scales, geometric fluctuations will cause temperature variations on all scales as well. For the purpose of quantifying the effects of these fluctuations, we construct a fractal of the prescribed dimension $D = 2.35$. It is constructed by a hierarchical procedure that is illustrated in Figure 2. We start with two points at a unit separation in a plane with coordinates x and y. Then, at every generation g, a copy of the entire structure is rotated an angle α around the end point.

The consecutive rotations illustrated in Figure 2 produce an ordered structure that is confined to the xy-plane. In order to introduce randomness as well as a structure that extends in three dimensions, two additional steps are added to the model: first, the replacement $\alpha \to \pm\alpha + \delta\alpha$, where $\delta\alpha$ is a random addition of zero mean and $\sqrt{\langle\delta\alpha^2\rangle} = \alpha/50$ is carried out. Second, an out-of-plane tilting by an average angle of $1/6$ is performed. This has the effect of giving the overall structure an envelope of aspect ratio $c/a = 1/6$ as indicated by the fitting of the 'Oumuamua light curves (Mashchenko 2019).

It should be noted that the present model does not represent the physics of the aggregation processes leading to fractal structures (Suyama et al. 2008; Wada et al. 2011; Okuzumi et al. 2012; Kataoka et al. 2013), but only seeks to capture the geometric fluctuations that are intrinsic to such fractals. It does, however, mimic the buckling process that is caused by colliding dust aggregates (Suyama et al. 2008), by prescribing an angle between connected particle chains, the smaller the angle, the larger the fractal dimension. To get the prescribed $D = 2.35$ value, an angle of $\alpha = 0.48\pi$ was used (see Appendix).

The fractal model is applied to represent the local thickness fluctuations in the z-direction: the xy-projection of particle density $\rho(x, y)$ defines the local thickness

$$L(x, y) = \frac{\rho(x, y)}{\overline{\rho}} 2c \tag{10}$$

where $\overline{\rho}$ is the average of $\rho(x. y)$, so that the average of L is $2c$. This local L-value is then taken as input in Equation (2) to obtain the local day- and night-side temperature shown in Figure 3, which also shows two optical images. Note that regions of high-infrared transparency exist on all scales.

However, observations by an infrared telescope are unlikely to resolve the level of detail shown in this figure. In order to determine the average effect of the geometric fluctuations inherent in a fractal, we may simply integrate the radiation over the xy-plane. Taking the fluctuations into account in this way, we may define the effective thermal thickness L_{eff} that gives the same radiation from a disk with constant thickness (see the Appendix). In the limit of large system sizes, an asymptotic value of L_{eff} is expected from the fractal nature of the geometry. In the Appendix, we obtain the value $L_{\mathrm{eff}} \approx 2c/5$, so, the fluctuation effect is large; it reflects the nonlinear relationship between T and L. Using the $L \to L_{\mathrm{eff}}$ replacement in Equation (2) allows for a one-dimensional calculation of the radiation at each moment in time as θ increases. This was done calculating the infrared light curves in Figure 4.

2.2. Condition for Observations

The reported sensitivity of the MIRI imager of the James Webb Space Telescope gives a signal strength at which the signal-to-noise ratio is 10 for an on-source integration time of 10 ks.[1] Reducing the integration time to 1 ks allows for the resolution of time variations on the timescale of 'Oumuamua's rotation period. This implies a corresponding increase in the noise floor by a factor of 10. In this case, curve fitting of the predicted MIRI noise floor s, yields the approximation

$$s = 10^{-32.0+2(\lambda-\lambda_0)/\Delta\lambda}\ \mathrm{W/(m^2Hz)} \tag{11}$$

[1] See Figure 1 in user documentation for the James Webb Space Telescope, MIRI sensitivity (https://jwst-docs.stsci.edu/jwst-mid-infrared-instrument/miri-predicted-performance/miri-sensitivity).

Figure 3. Optical day-side and infrared night-side (bottom figure) radiation from the geometric CFA model of 'Oumuamua using 8 million particles. The day-side images correspond to $\theta = 0'$ and $30'$ in Figure 1, while the infrared image is a night-side view of the $\theta = 0'$ orientation.

where λ is the wavelength of the observed radiation, $\lambda_0 = 4.0$ μm and $\Delta\lambda = 18.5$ μm. To get the comparable prediction of the signal strength, we use the wavelength of maximum intensity $\lambda_m(T) = b/T$, where $b = 2.9\ 10^{-3}$ K m is the constant of the Wiens displacement law. The standard Planck spectrum

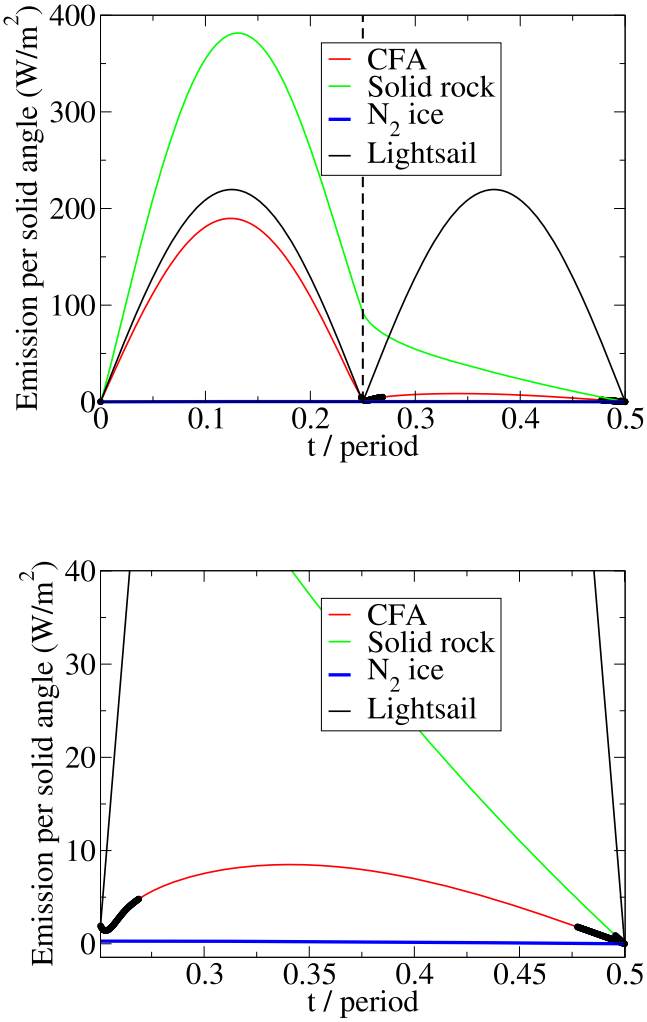

Figure 4. Top figure: infrared signals in the direction of earth from the different models over half a period of rotation. The vertical line shows the transition from the day to night side, and the thick black line mark where the signal falls below the sensitivity levels of MIRI. The observational distance is 0.16 au. Bottom figure: zoom-in of the night-side infrared signal.

then gives

$$I_m(T) = 2\frac{|\sin(\theta(t))|h\nu_m^3(T)}{c_0^2(e^{hc/(kb)} - 1)}\left(\frac{a}{R_o}\right)^2 \tag{12}$$

where $\nu_m(T) = c/\lambda_m(T)$, h is Planck's constant, c_0 is the speed of light, and $R_o = 0.16$ au is the observation distance.

2.3. Predicted Infrared Signals for Different Models

Figure 4 shows the result for all four models over half a period, beyond which all curves repeat themselves. All thermal models are run for a number of initial rotations until their light curves have converged to steady-state values. Only the rock model maintains an internal temperature below the diffusion skin depth. However, changing this internal temperature only changes the surface temperature by $\sim$1 K, and the steady-state values are reached to within $\sim$1% by three rotation periods.

Except for the ice model signal, which falls below the detection level at all times, the signals are masked by a black line wherever they fall below the detection level. This level is defined by the temperature where $I_m(T) < s$, where the

sensitivity s is defined in Equation (11) and I_m, the predicted intensity, is given in Equation (12).

Most notably, while the rock model displays a steady signal decay over the night-side period, the CFA model produces a second observable maximum. This is the case for the light-sail model as well, but this signal is easily recognizable since the day- and night- side maxima have the same values. Also, only the rock model with its significant heat capacity has a detectable signal at $t =$ period $/4$, at which point the CFA becomes invisible in the infrared region.

3. Discussion

Having identified a set of crucial measurements that distinguish between the different hypothesis for the structure of the next 'Oumuamua object using the existing James Webb Space Telescope has clear advantages. Technical solutions for chasing it with a dedicated spacecraft that could make close observations, have been suggested (Seligman & Laughlin 2018; Hibberd & Hein 2020) and will be much more challenging.

Analysis of 'Oumuamua light curves indicates a tumbling rotational state (Drahus et al. 2018; Fraser et al. 2018), and the different 'Oumuamua models are all likely to result in a such a state. The models that rely on the radiation pressure to explain the extra-gravitational acceleration would likely acquire such a state from the YORP effect (Rubincam 2000). In the rock models where the acceleration is caused by outgassing, a tumbling state would likely result from the torque created by the gas pressures (Rafikov 2018). Also, in the case of the rock model, a tumbling state may have survived interstellar travel (see Burns & Safranov 1973) from lack of internal dissipation caused by rotational deformation. Such tumbling has not been included in our calculations, yet these calculations show that the infrared signals from the different 'Oumuamua models will be qualitatively different.

Different shapes and rotational states will affect both the infrared and optical signals. In the case of the oblate ellipsoidal shape, which emerged as the more likely one for 'Oumuamua (Mashchenko 2019), there is significant rotation around a minor principal axis (the major principal axis being associated with the maximum moment of inertia). This explains the large light-curve variations since rotation purely around the major principle axis would cause no light-curve variations at all.

In the case of a prolate shape, rapid rotation around a minor principal axis could make the corresponding rotation period shorter than the thermal relaxation time. This would blur out the infrared signal variations since the temperature would then even out on the different sides, thus making the signals from the CFA and rock models similar. However, this behavior would be predictable from a proper inversion of the light-curve data with respect to the rotational state. So, the cases where the infrared signal is less effective as a tool to discern the different models are identifiable.

Optical observations that constrain the shape and rotational state of the object (Mashchenko 2019) will therefore make it possible to obtain correspondingly different predictions for the infrared signal of the different models, thus making it possible to distinguish between them. The main difference between the infrared predictions for the different models is most pronounced in the night-side signal where the CFA model produces a weaker maximum that is not present in the other models. Since this maximum is only a factor of 2 above the 10 SNR noise floor at an observation distance of 0.16 au (the closest approach of 'Oumuamua), the distinction possibility is limited to near-Earth observations.

We thank Jane X. Luu and Renaud Toussaint for early discussions on this work as well as the Research Council of Norway through its Centers of Excellence funding scheme, project number 262644.

Appendix

A.1. Fractal Model

The fractal dimension is obtained by noting that the overall size of the structure is increased by a factor $(2 - 2\cos\alpha)$ as $g \to g + 1$, while the number of links in the structure increases by a factor 2. At generation number g, the total size of the structure $L_g = (2 - 2\cos\alpha)^g$ and the number of links $M_g = 2^g$. Eliminating g between these two equations yields $M = L^D$ where the fractal dimension

$$D = \frac{\ln 4}{\ln(2 - 2\cos\alpha)}, \tag{A1}$$

or, equivalently $\cos\alpha = 1 - 2^{(2-D)/D}$.

Figure 5(a) plots the particle number as a function of distance from the $g = 1$ starting position for a system of 8 million particles. It shows that the behavior is indeed fractal over 2–3 orders of magnitude. The crossover behavior at large scales happens as r approaches the system size.

The number of particles in an object like 'Oumuamua is about 8 orders of magnitude larger than in our simulations; a simulation of such particle numbers is beyond the capacity of any existing computer. However, relative numbers, such as the volume fraction of regions that have a certain fraction of the average density, will be constant in systems large enough to avoid significant finite size effects. The general reason for this is that a crossover at a certain scale would define a length scale which is different from both the system size and the particle size, and the defining feature of a fractal is exactly that it lacks such intermediate scales.

In the insert of Figure 5(a) the fraction of sites that contain less than 10% of the average particle number after projection into the plane that contains the largest semimajor axis a and b is plotted. The particular number 10% is chosen arbitrarily to define regions that are significantly thinner than the average, the point being that this fraction approaches an asymptotic value already at a particle number of a million. Below that number, the average number of projected particles is sometimes below 10, which makes it impossible for a non-zero particle number to be below 10%. This is a finite size effect. Figure 5(a) also plots the fraction of projected particle numbers that equal one. This fraction decays as a power law with an extrapolation to a few parts per thousand at the size of 'Oumuamua ($M \sim 10^{18}$), which shows that only a very small fraction of the fractal will contain sites that emit infrared radiation without further scattering. This further justifies the assumption of a local equilibrium between massive particles and radiation.

A.2. Photon Mean Free Paths in a Fractal

In the following, we derive the mean free paths λ of a photon emitted from a solid site on a fractal of dimension D and the mean free path of one starting from an arbitrary location, starting with the former. In order to do this, we first consider

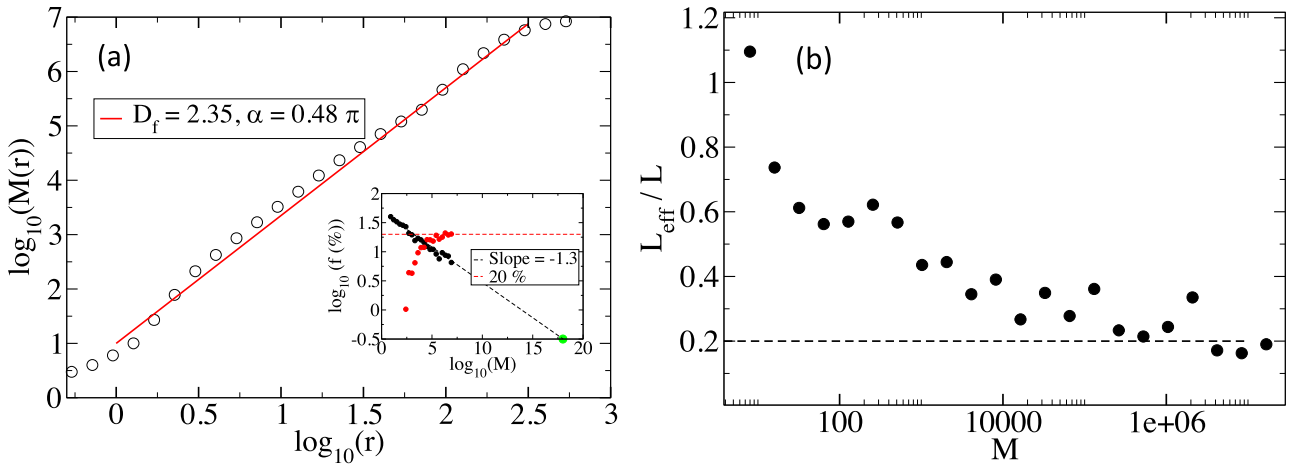

Figure 5. (a) The number of particles (mass) of the fractal structure as a function of distance from the initial $g = 1$ structure. The red line has a slope of 2.35. The insert shows results from projections of the fractal particle structure into the xy-plane. Black dots show the fraction of sites f that contain only one particle and red dots the fraction of sites that contain less than 10% of the average particle number. The green dot shows the extrapolation to the number of particles in an 'Oumuamua-sized fractal. (b) The average effective thermal thickness as a function of system size.

the probability $P_0(r)$ of an emitted photon not hitting another particle of radius r_0 over a distance r. If we split this distance into n segments, each of length $\Delta r = r/n$, we can write $P_0(r)$ as the product of the probabilities of not hitting a particle in each of these segments:

$$P_0(r) = \prod_{i=0}^{n} (1 - \pi r_0^2 \rho_N(r_i)\Delta r). \tag{A2}$$

Here $r_i = i\Delta r$ and $\rho_N(r)$ is the number density of particles so that $\Delta r \pi r_0^2 \rho_N(r_i)$ is the average number of particles in the volume $\Delta V = \Delta r \pi r_0^2$. This small average particle number equals the probability of the photon stopping inside this volume, and consequently, the expression in parentheses in Equation (14) is the probability of not hitting a particle inside ΔV.

Now, taking the log of Equation (14) gives

$$\begin{aligned} \ln P_0(r) &= \sum_i \ln(1 - \pi r_0^2 \rho_N(r_i)\Delta r) \\ &\approx -\textstyle\sum_i \pi r_0^2 \rho_N(r_i)\Delta r \\ &\approx -\int_{r_0}^{r} dr' \pi r_0^2 \rho_N(r') \end{aligned} \tag{A3}$$

where we have used the approximation $\ln(1 - x) \approx -x$ for $x \ll 1$ in going from the first to the second line, and taken the $\Delta r \to 0$ limit in passing to the last line. Exponentiating gives

$$P_0(r) = e^{-\int_{r_0}^{r} dr' \pi r_0^2 \rho_N(r')}. \tag{A4}$$

Over the distance r the photon will either be absorbed or not. So, the probability of being absorbed between r_0 and r is therefore $P(r) = 1 - P_0(r)$. The probability $p(r)dr$ of being absorbed between r and $r + dr$ is therefore

$$p(r)dr = P(r + dr) - P(r) = P'(r)dr. \tag{A5}$$

Note that $p(r)$ is also the distribution of the mean free paths, which we can now write as

$$p(r) = \pi r_0^2 \rho_N(r) e^{-\int_{r_0}^{r} dr' \pi r_0^2 \rho_N(r')} \tag{A6}$$

by using Equations (16) and (17). The mean free path is then given by

$$\lambda = \int_{r_0}^{\infty} dr r p(r). \tag{A7}$$

Using the fact that the number density around a particle in a fractal of dimension D is (Flekkøy et al. 2019)

$$\rho_N(r) = \frac{3}{4\pi r_0^3}\left(\frac{r}{r_0}\right)^{D-3}, \tag{A8}$$

the exponent in Equation (18) becomes

$$\int_{r_0}^{r} dr' \pi r_0^2 \rho_N(r') = -\frac{3}{4(D-2)}\left(\left(\frac{r}{r_0}\right)^{D-2} - 1\right) \tag{A9}$$

and with the substitution $x = r/r_0$, we find the mean free path

$$\lambda = r_0 \int_1^{\infty} dx x^{D-2} e^{-\frac{3}{4(D-2)}(x^{D-2}-1)}, \tag{A10}$$

which we can write as $\lambda = I(D) r_0$, where the prefactor $I(D) \sim 1$ as long as $D > 2$. When $D < 2$, however, $I = \infty$, and $I \to \infty$ as $D \to 2^+$. For $D = 2.35$, as in our case, $\lambda \sim r_0$.

The probability $P_0(a)$ that a photon originating inside the structure will escape over a distance $\sim a$ is given by Equation (16), which gives

$$P_0(a) = e^{-\frac{3}{4(D-2)}\left(\left(\frac{a}{r_0}\right)^{D-2}-1\right)}, \tag{A11}$$

which is extremely close to zero as $(a/r_0)^{D-2} \sim 10^5$.

The mean free path of a photon starting from an arbitrary point on a surface that cuts through the fractal is not determined by the mass density surrounding a solid point, but rather the average density on that surface. This surface, as well as cross sections parallel to it, will have an average number density of particles

$$\rho_N(a) = \frac{3}{4\pi r_0^3}\left(\frac{a}{r_0}\right)^{D-3}. \tag{A12}$$

In order to estimate the mean free path $\overline{\lambda}$ from such a surface, we require that the volume $\overline{\lambda}\pi r_0^2$ be equal to the average

volume per particle $1/\rho_N(a)$. This gives

$$\overline{\lambda} = \frac{1}{\pi r_0^2 \rho_N(a)} = \frac{4\pi r_0}{3}\left(\frac{a}{r_0}\right)^{3-D}. \tag{A13}$$

A.3. Fractal Fluctuations and the Effective Heat Thickness L_{eff}

The thickness fluctuations of the fractal CFA model will cause local temperature fluctuations. By averaging the corresponding radiation σT^4 from the surface, it is possible to define an effective thickness $L_{\rm eff}$ that produces the same radiation from a disk of that thickness. For the CFA model, where the thermal diffusion length exceeds the thickness $2c$, a steady-state assumption is justified, in which case we may replace the temperature gradients in the boundary conditions by the approximation

$$\frac{\partial T(L,\, t)}{\partial z} \approx \frac{Tb - T_f}{L(x,\, y)}, \tag{A14}$$

where T_f and T_b are the front- and backside surface temperatures. Then the steady state is described by the energy balance

$$\begin{aligned}(1 - p) j_{\rm sun} \cos\theta(t) &= \sigma T_f^4 - \kappa_t \frac{T_f - T_b}{L(x,\, y)} \\ \kappa_t \frac{T_f - T_b}{L(x,\, y)} &= \sigma T_b^4,\end{aligned} \tag{A15}$$

where T_f is the day-side temperature and T_b the night-side temperature. Indeed, solving the full diffusion Equation (1) with the CFA parameters gives temperature profiles $T(x,\, t)$ that are quite linear in x, justifying the use of Equation (27) in calculating $L_{\rm eff}$. Figure 5(b) shows how this effective thickness varies with system size. In these calculations, $L_{\rm eff}$ was averaged over 20 different structures for each system mass M. The fact that it converges to an approximate asymptotic value indicates that the simulations are in the proper large-size regime.

So, Equations (27) were used as an approximation to produce Figure 3. In the calculations that produced the temperature values in Figure 4 the substitution $L \to L_{\rm eff}$ was used in Equation (2) to represent the net effect of local variability in the transmission of heat.

ORCID iDs

Eirik G. Flekkøy https://orcid.org/0000-0002-6141-507X

References

Bannister, M. T., Bhandare, A., Dybczynnski, P. A., et al. 2019, NatAs, 3, 594
Bialy, S., & Loeb, A. 2018, ApJL, 868, 5
Burns, J., & Safranov, V. 1973, MNRAS, 165, 403
Cooper, J., Christian, E., Richardson, J. D., & Wang, C. 2003, EM&P, 92, 261
Ćuk, M. 2018, ApJL, 852, L15
Desch, S. J., & Jackson, A. P. 2021, JGRE, 126, e06807
Drahus, M., Guzik, P., Waniak, W., et al. 2018, NatAs, 2, 407
Fitzsimmons, A., Snodgrass, C., Rozitis, B., et al. 2018, NatAs, 2, 133
Flekkøy, E., Luu, J. X., & Toussaint, R. 2019, ApJL, 885, L41
Fraser, W. C., Pravec, P., Fitzsimmons, A., et al. 2018, NatAs, 2, 383
Harris, A. W. 1998, Icar, 131, 291
Havlin, S., & Ben-Avraham, D. 2002, AdPhy, 51, 187
Hibberd, A., & Hein, A. M. 2020, AcAau, 179, 594
Jackson, A. P., & Desch, S. J. 2021, JGRE, 126, e06706
Jewitt, D., & Luu, J. 2019, ApJL, 886, L29
Jewitt, D., Luu, J., Rajagopal, J., et al. 2017, ApJL, 850, L36
Kataoka, A., Tanaka, H., Okuzumi, S., & Wada, K. 2013, A&A, A4, 554
Luu, J. X., Flekkøy, E. G., & Toussaint, R. 2020, ApJL, 900, L22
Luu, J. X., Xiao-Ping, & Jewitt, D. 2019, ApJ, 158, 220
Mashchenko, S. 2019, MNRAS, 489, 3003
Meech, K. J., Weryk, R., Micheli, M., et al. 2017, Natur, 552, 378
Merril, R. 1969, Radiative heat transfer, Tech. rep., NASA, https://ntrs.nasa.gov/api/citations/19710021465/downloads/19710021465.pdf
Micheli, M., Farnocchia, D., Meech, K., et al. 2018, Natur, 559, 223
Moro-Martín, A. 2018, ApJ, 866, 131
Moro-Martín, A. 2019, AJ, 157, 86
Okuzumi, S., Tanaka, H., Kobayashi, H., & Wada, K. 2012, ApJ, 752, 106
Olsen, K. S., Flekkøy, E. G., Angheluta, L., et al. 2019, NJPh, 21, 063020
O'Shaughnessy, B., & Procaccia, I. 1985, PhRvL, 54, 455
Rafikov, R. 2018, ApJL, 867, 17
Raymond, S. N., Armitage, P. J., Veras, D., Quintana, E. V., & Barclay, T. 2018, MNRAS, 476, 3031
Rubincam, D. P. 2000, Icaros, 148, 2
Seligman, D., & Laughlin, G. 2018, AJ, 155, 217
Seligman, D., & Laughlin, G. 2020, ApJL, 896, L8
Suyama, T., Wada, K., & Tanaka, H. 2008, ApJ, 684, 1310
Trilling, D. E., Mommert, M., Hora, J. L., et al. 2018, ApJ, 156, 261
Wada, K., Tanaka, H., Suyama, T., Kimura, H., & Yamamoto, T. 2011, ApJ, 737, 36
Williams, G. 2017, Comet C/2017 U1 (panstarrs), Tech. rep., MPEC 2017-U181, https://minorplanetcenter.net//mpec/K17/K17UI1.html
Zhang, Y., & Lin, D. N. C. 2020, NatAs, 4, 852